GEOPHYSICS®

Inferring Hydraulic Connectivity of Induced Fractures in the Near-wellbore Region Using DAS-recorded Tube Waves Excited by Perforation Shots

Journal:	*Geophysics*
Manuscript ID	GEO-2021-0276.R2
Manuscript Type:	Technical Paper
Keywords:	DAS (distributed acoustic sensors), hydraulic fracturing, tube wave, borehole geophysics
Manuscript Focus Area:	Borehole Geophysics, Reservoir Geophysics

DOI:10.1190/geo2021-0276.1

INFERRING HYDRAULIC CONNECTIVITY OF INDUCED FRACTURES IN THE NEAR-WELLBORE REGION USING DAS-RECORDED TUBE WAVES EXCITED BY PERFORATION SHOTS

Harrison Schumann, Colorado School of Mines, 1500 Illinois St, Golden, CO 80401, hschumann@mymail.mines.edu

Ge Jin, Colorado School of Mines, 1500 Illinois St, Golden, CO 80401, gjin@mines.edu

DOI:10.1190/geo2021-0276.1

Original paper date of submission: 1 May, 2021

ABSTRACT

We present a novel use of tube waves exited by perforation (or "perf") shots and recorded on distributed acoustic sensing (DAS) to infer and compare the hydraulic connectivity of induced fractures near the wellbore on a stage-by-stage basis. Evaluating the fracture connectivity near the wellbore is critical since it controls the flow of the hydrocarbons from the formation to the wellbore. Currently, there are no established methods used to assess this property. However, we discuss how tube wave decay rates can be used to infer relative differences in fracture connectivity between stages and, through field observations on DAS, demonstrate the correlation between decay rates and frac effectiveness. Additionally, we consider other potential uses of this data in unconventional wells such as assessing plug integrity and constraining fracture geometry with Krauklis waves. DAS data is commonly acquired during the perf shots but primarily for fiber depth calibration purposes and has not been well studied. Our work illustrates the untapped potential of this data and how it can be easily repurposed to bring new insights about fracture characteristics in the near-wellbore region.

DOI:10.1190/geo2021-0276.1

INTRODUCTION

Over the past decade, unconventional petroleum resources have become increasingly important assets for oil and gas production. Production performance in unconventional wells is not only affected by the rock quality but also by the characteristics of the fractures induced by the hydraulic fracturing process. Characteristics such as length, height, orientation, and hydraulic connectivity with the wellbore play an important role for enabling flow of hydrocarbons from the surrounding rock to the well. Understanding these properties at the stage level in a multistage well is crucial for assessing frac effectiveness and optimizing development in unconventional reservoirs. Over the past decade, fiber optic sensing has shown enormous value for this exact purpose. Fiber optic cables can be permanently mounted outside the casing, mechanically coupling with the both the formation and the wellbore, which enables continuous monitoring of both the well and the formation. Fiber optic cables can be used to record both distributed acoustic sensing (DAS) as well as distributed temperature sensing (DTS) using backscattered light pulses sent from a laser interrogator (Hartog, 2017). Both DAS and DTS have shown immense value for unconventional wells and have been used for microseismic monitoring (e.g., Binder and Chakraborty, 2019), for detecting interwell fracture hits (e.g., Jin and Roy, 2017), for vertical seismic profiling (VSP) (e.g., Binder et al., 2019), and for identifying fracture initiation points (e.g., Sookprasong et al., 2014), among others.

Although there are many established methods of fracture characterization for the far-field region, there are relatively few for the near-wellbore region, which extends from the wellbore up to several meters into the formation. The near-wellbore region has a profound impact on production since this region controls the flow between the hydrocarbons in the far-field and the wellbore. Ugueto et al. (2019) used DAS, DTS, and downhole pressure gauges to estimate the near-wellbore fracture geometries and demonstrate the importance and complexity of this region. However, fracture geometry does not provide an indication of the hydraulic connectivity between the fracture and the wellbore, which is more directly related to production. There are currently no established methods used to estimate this hydraulic connectivity at the stage level. However, in this paper we propose the use of tube waves initiated by perforation (or “perf”) shots and recorded on DAS as a means of assessing the hydraulic connectivity near the wellbore of the induced fractures stage-by-stage.

DOI:10.1190/geo2021-0276.1

The perf shot refers to the ignition of the perforation gun in the borehole and, as the name implies, is used to create perforations in the casing of the well. These perforations are typically created in clusters ("perf clusters") along the horizontal length of the stage to enable the frac fluids to stimulate the formation evenly. The well for this study utilized what is known as plug-and-perf completion design. With this design, each of the stages in the well began with dropping the plug seat and the perf gun into place. The perf gun was then ignited multiple times along the stage length, creating evenly spaced perforation clusters. Next, the plug ball was dropped into the plug seat, sealing the current stage from the previous one and the frac fluids were then pumped into the well to hydraulically fracture the reservoir. This process was repeated for each stage sequentially from the toe to the heel of the well.

Tube waves (or borehole Scholte waves) are a type of guided wave that travel along the solid-liquid interface of the borehole wall. Although tube waves have not been well studied on DAS, these waves have shown potential use for fracture characterization in both laboratory experiments (Zlatev et al, 1988) and in the field when recorded on wellhead sensors (Dunham et al., 2017) or downhole hydrophone arrays (Hunziker et al., 2019). Tube waves have also been observed on both surface and downhole geophone arrays (e.g., Li et al., 2017; Bergery et al., 2017). The potential of these waves for fracture characterization is due their relationship with hydraulic impedance and flow communication between fractures and the wellbore. Hydraulic impedance is defined as the ratio of pressure to volumetric flow rate and fractures hydraulically connected with the borehole will create a boundary of hydraulic impedance contrast (Holzhausen and Gooch, 1985). Tube waves that cross such a boundary will attenuate (and reflect) as a function of the

DOI:10.1190/geo2021-0276.1

magnitude of the contrast due to the change in boundary conditions and the dissipation of energy into the fracture. As such, the amplitudes of tube waves generated by the perf shot and transmitted across a previously stimulated stage may be used to infer the hydraulic connectivity between the wellbore and the induced fractures along the perf clusters.

In addition to field and laboratory observations, other works have used numerical methods to examine the relationship between tube waves and induced fractures intersecting the wellbore. Bakku et al. (2013) used numerical solutions to study the attenuation of tube waves as a function of frequency and fracture properties such as width. The authors found that for frequencies above 250 Hz, larger fracture widths significantly reduce the transmission coefficient of tube waves. Similarly, Zhang et al. (2021) used finite-difference elastic modeling to study the full seismic wavefield in the wellbore following an explosive source to assess the difference in tube wave attenuation when encountering a fracture versus an unstimulated perf hole. The numerical model showed that for frequencies above 250 Hz, the attenuation was higher for fractures than for unstimulated perf holes. The results from these studies indicate that the tube waves observed on DAS could be a promising means for evaluating completion effectiveness.

Figure 1 shows a simplified visual model for the phenomenon described above. In this model, the perf gun generates tube waves that propagate towards both the toe and the heel of the well and are recorded on the wellbore-coupled DAS fiber. The tube waves in the heel-ward direction experience little change in amplitude since the are no considerable contrasts in the hydraulic impedance along the wellbore. However, in the toe-ward direction the tube waves transmitted across the prior stage attenuate quickly due to the hydraulic impedance contrast and

DOI:10.1190/geo2021-0276.1

dissipation of energy related to the induced fractures along the perf clusters. As demonstrated by this model, we want to utilize the amplitudes of transmitted tube waves generated by the perf shot and recorded on DAS in our study well to infer fracture connectivity in the prior stage.

To our knowledge, this is the first work to examine the use of tube waves for fracture characterization when either recorded on DAS or generated by the perf shot. Since a DAS array consists of closely spaced channels with known positions along the entire length of the borehole, the spatial uncertainty is low, and the spatial resolution is quite high. Additionally, since the fiber is located outside the casing, there is no interference on the tube waves from the instrument. These qualities make DAS better suited to studying tube waves than other instruments such as wellhead sensors or downhole hydrophone arrays. Additionally, although tube waves can be generated in unconventional wells by other sources such as surface Vibroseis trucks (Bakku et al., 2013) and changes in pumping rates at the wellhead (Dunham et al., 2017), perf shots are ideal sources for studying fracture connectivity using tube waves because of the proximity of the perf gun to the prior stage, the multiple shots per stage, and the large tube wave amplitudes that are generated. Since the perf shot is a part of the completion process and DAS data are often recorded during the perf shot for depth calibration purposes regardless, it is an extremely cost-effective tube wave source for wells equipped with DAS.

The purpose of this work is two-fold: first, to introduce some interesting observations from the DAS data recorded during the perf shot, and second, to demonstrate the unexploited value of tube waves in this data for the use of fracture characterization. We will begin by going over the details of the study well, completion design, and DAS data acquisition. Following this, we will

DOI:10.1190/geo2021-0276.1

show an example of a typical wavefield recorded on DAS following a perf shot, pointing out some critical observations and comparing the field data with the expectations from our proposed model in Figure 1. We will then describe the methodology used to quantify the relative differences in tube wave decay which will serve as a proxy for comparing the fracture connectivity between stages. Next, we will show an example of two stages from the study well with quite different results followed by a discussion about potential interpretations of the observed differences. Lastly, we will consider other prospective uses for this type of DAS data (such as identifying plug failure and constraining fracture lengths using Krauklis waves) in addition to examining relevant limitations of the observations.

DATA AND OBSERVATIONS

The data for this study come from a horizontal, unconventional well located in the Northern Denver-Julesburg (DJ) basin. This well is owned and operated by Bonanza Creek Energy (through merger with HighPoint Resources) and targets the Codell Sandstone, a low-permeability reservoir that is a prolific source of hydrocarbons in the DJ basin. The well is equipped with a fiber optic cable that recorded both DAS and DTS data during all phases of completion. A primary goal for this well was to evaluate the impact of various completion variables and find the optimal completion design for future development in surrounding acreage. Since DAS and DTS can enable the evaluation of frac effectiveness at the stage level, completion variables such as stage length, number of clusters per stage, total proppant volume, total fluid volume, fluid type, and pumping rate were varied across the 76 stages completed in this well. The DAS data were acquired using a sampling rate of 10 kHz, approximately 1 m channel spacing, and an estimated gauge length of 1

DOI:10.1190/geo2021-0276.1

m (the recorded gauge length was not available due to loss of some metadata). Gauge length, in simple terms, refers to the distance along the fiber over which strain is measured for each of the channels. Originally, the operator recorded DAS data during the perf shots originally as a way to QC the depths of both the perforation clusters and the plugs during completion. As such, this work presents an economical method of exploiting the untapped potential of this DAS data in order to provide new insights into the characteristics of induced fractures stage-by-stage in unconventional wells.

Figure 2 displays an example wavefield and RMS amplitude profile that is characteristic of the DAS data recorded during the perf shot. In this data, we typically observe both P-waves and tube waves (as marked on the figure), and occasionally S-waves. The tube waves have significantly higher amplitudes than the P-waves, and, though the P-waves decay almost symmetrically in both directions from the source, the tubes decay quite asymmetrically. In the direction of the heel, the tube waves maintain high amplitudes even at great distances from the perf gun and can even be observed reflecting from the surface and propagating back down the borehole (for some stages that would be a combined distance of more than 10 km). However, in the toe-ward direction, the propagating tube waves often do not even reach the plug of the prior stage (less than 75 m in distance). This remarkable difference in tube wave decay rates between the two propagation directions is most prominent between the plug seat of the current stage and the plug of the previous stage. Within this range, the recorded tube wave energy decays rapidly compared to the rate observed in the heel-ward direction.

DOI:10.1190/geo2021-0276.1

The field observations from Figure 2 align well with the expectations from our proposed model in Figure 1. As illustrated in the model, we would expect the tube waves propagating in the heel-ward direction to decay at an extremely low rate due to a lack of hydraulic impedance contrasts along the wellbore. Conversely, in the toe-ward direction we would expect that the tube waves decay rapidly within the prior stage due to the hydraulic impedance contrast of the induced fractures. These expected behaviors are consistent with what we observe in the field data. Because of this agreement between our model and field observations, we believe that the tube wave decay in the toe-ward direction is highly related to the connectivity of induced fractures within the prior stage. Therefore, by quantifying the tube wave decay rate in each stage we believe we can compare the connectivity of fractures between the stages of our study well.

DOI:10.1190/geo2021-0276.1

METHODOLOGY AND RESULTS

We used the methodology described in this section and visualized in Figure 3 to create a numerical representation of the tube wave decay rate for each stage so that we could compare the fracture connectivity between the stages in our study well. We first apply a linear moveout (LMO) at the tube wave velocity (1494 m/s) in both directions from the perf gun source to flatten the tube wave arrivals for each perf shot record. Then, we use a 100 ms time window starting just before the tube wave first arrival to isolate the tube waves from the body waves. Lastly, we calculate the log of the average amplitude within the time window for each channel and fit a line using the least squares method between the plug seat of the current stage and the plug of the prior stage. The slope of this line served as the numerical representation of the tube wave decay rate, which is positively correlated with the fracture connectivity for the stage.

Figure 4 shows an example of both the wavefield (after LMO) and logarithmic decay profile of two stages that had very different decay rates calculated using the methodology described previously. Stage 22 exhibits a more rapid tube wave decay with the line fit to the log of the average amplitudes having a slope of -0.0708 dB/m. On the other hand, stage 32 exhibits a less rapid decay with a slope of only -0.0042 dB/m. The stark difference between these two stages is readily apparent not just from the logarithmic decay curves but also from the wavefields as well. In stage 22, the tube wave signal is fully decayed when by around the middle of the stage. In stage 32, however, the tube wave signal maintains high amplitudes throughout the entire length of the stage and even remains present in the form of reflections primarily between the first cluster (the cluster with the greatest measured depth) and the perf gun. As mentioned previously, tube waves will reflect when encountering a contrast in hydraulic impedance. In stage 32, these reflections propagate back and forth across the stage several times over and can be observed several hundred milliseconds after the first arrival. Since these two stages are identical in length, the tube wave first arrivals and subsequent reflections in stage 32 travel a combined distance many times greater than the tube waves in stage 22 before fully decaying.

DISCUSSION

Given the proposed supposition that tube wave decay is highly related to the presence and connectivity of fractures within a given stage, the significant differences in tube wave behavior in stages 22 and 32 (shown in Figure 4) suggest that the fractures in stage 32 either had considerably less connectivity than those in stage 22 or potentially were never even initiated. When comparing

DOI:10.1190/geo2021-0276.1

only the completion design of these two stages, which were quite similar, such contrasting outcomes would not be expected. Stages 22 and 32 had identical stage lengths, perf cluster spacing, and total number of perforations at each cluster and were treated with comparable amounts of proppant, fluid volumes, and pumping rates. Additionally, both stages utilized a reverse hybrid frac in which a high-viscosity fluid was first pumped to initiate the fractures followed by a low-viscosity fluid used to place the proppant. The only notable difference in completion design between stages 22 and 23 was related to changes in proppant concentrations during the pumping schedule. Stage 22 was completed using a constant proppant concentration throughout the entire duration of proppant injection whereas in stage 32 the proppant concentration was first increased stepwise to a predetermined max value and then dropped to a constant level for the remainder of the pumping. However, we do not believe the difference in proppant concentration and loading during treatment was a significant controlling factor causing the apparent difference in fracture connectivity. The 12 stages completed using a reverse hybrid step-up proppant concentration design had a mean calculated decay rate of -0.0311 dB/m and the six stages completed with the reverse hybrid constant proppant concentration design had mean value of -0.0320 dB/m. Given the similarity in these values, we do not believe that the disparities in proppant concentration and loading schedules during completion is responsible for the observed differences between stages 22 and 32.

Although the completion parameters for stages 22 and 32 were nearly identical, the calculated uniformity index (UI) for each stage was quite different. UI is a statistical metric from 0 to 100% that indicates the consistency of flow distribution among the perf clusters during the

DOI:10.1190/geo2021-0276.1

hydraulic fracturing process as estimated by the high frequency noise amplitudes recorded on DAS during the stimulation. The formula for UI is

$$UI = 100 \times \left(1 - \frac{s(q_i)}{\bar{q}}\right), \qquad (1)$$

where q_i is the flow volume for each perf cluster in the stage, $\bar{q}$ is the mean flow volume of the perf clusters, and s is the standard deviation. The closer the UI is to 100%, the more even the fluid placement was along the perf clusters in a stage. Figure 5 shows the UI for both stage 22 and 32 as well as the estimated fluid distributions from which the UI was calculated. As we can see from the figure, the flow distribution in stage 22, which had a UI of 80.2%, appears to be much more even across all six perforation clusters with only a slight heel bias. However, in stage 32, which had a UI of 23.8%, the flow appears to be less evenly distributed with cluster 1 seeming to have taken the majority of the fluid.

The discrepancy in UI may explain the vastly different tube wave decay rates calculated for stages 22 and 32. In stage 22, the apparent evenness of the stimulation among the perf clusters suggests that fractures were likely initiated at most if not all of the perf clusters with good connection to the wellbore. If this is the case, then we would expect the rapid tube wave decay observed in stage 22. Conversely, in stage 32 we saw that the majority of the fluid seemed to be taken by cluster 1. This indicates that the other clusters in the stage were not stimulated effectively; fractures might not have even been induced at these other clusters. As noted earlier, we also observe reflected tube waves in Figure 4c at cluster 1 but not at the other clusters. These reflected tube waves indicate the presence of a connected fracture at cluster 1, providing additional supporting to the observations from the flow data. Given this assessment of the frac effectiveness

DOI:10.1190/geo2021-0266.1

in stage 32, we would not expect significant tube wave decay to occur within this stage, especially since cluster 1 is located at the toe-ward end.

Although a low UI can result from a number of causes related to reservoir variability, stress shadowing, completion design, and completion execution, we suspect plug failure at stage 32 to be a major factor in this case. Figure 6 shows the temperature profile using DTS during the treatments of stages 30-32, which can help us understand how the fluids are distributed during treatment. Since the injected fluid is of a lower temperature than the surrounding reservoir, the fluid appears as a low temperature anomaly during treatment and gradually increases in temperature overtime. We can clearly see in Figure 6 that the fluid during stage 32 reaches the same measured depths as the fluid during stage 31. This indicates that the plug for stage 32 is ineffective and that stage 32 is losing fluid to stage 31.

The plug failure in stage 32 seems to have had a quite detrimental impact on the frac effectiveness as indicated from both the UI and the tube wave decay. We can visualize this impact in Figure 7 which shows the phase power of the high-frequency (500-5000Hz) data recorded on DAS during the treatment of stage 32 that was used for the UI and flow distribution estimations. From this figure, we observe that the phase power recorded along the clusters in stage 31 was actually higher than that recorded for the clusters in stage 32 apart from cluster 1. This indicates that the treatment fluid was primarily restimulating the clusters in the previous stage rather than stimulating the clusters in the current stage. Therefore, most of stage 32 was left effectively untreated due to the plug failure.

DOI:10.1190/geo2021-0276.1

Despite the similarities in completion design between stages 22 and 32, the actual effectiveness of the frac between these two stages was evidently quite dissimilar. The analysis of both the high-frequency DAS and DTS data indicates that stage 32 had operational issues and was therefore poorly stimulated in comparison to stage 22. This difference in frac effectiveness is clearly observable from the tube wave decay rates within each stage, providing further evidence of the relationship with fracture connectivity. Additionally, the high-frequency DAS data also indicated that cluster 1 in stage 32 was the only effectively stimulated cluster within that stage. The tube wave reflections observed at cluster 1 in Figure 4 show that the perf shot wavefield not only contains useful information about the induced fractures on a stage level but on a cluster level as well.

Although the primary focus of this work has been on the use of tube wave decay for inferring the connectivity of fractures stage-by-stage, we also want to discuss additional uses of this type of data. With the plug failure in stage 32 in mind, another observation from the tube wave data becomes relevant in this context: the propagation of the tube waves past the plug in stage 32. Figure 8c shows the perf shot wavefield for this stage again, this time with a greater distance beyond the plug seat displayed. Since tube waves travel along the solid-liquid interface between the borehole wall and the frac fluid, we would expect that a hydraulically sealed plug can reflect the majority of the tube wave energy. Therefore, plug failure may explain the propagation of tube waves past the plug in stage 32. This interpretation can be further supported by the data from stage 31. In Figure 6, it appears that the plug for stage 31 is properly sealing the fluids from stage 30 during treatment. Consequently, despite the tube waves in Figure 8a reaching the stage 31 plug with still relatively high amplitudes, the waves quickly decay after the plug. As demonstrated by

DOI:10.1190/geo2021-0276.1

this example, the interaction between tube waves and the plug may also be used to identify or confirm plug failure.

Another potential use for the perf shot data is the analysis of Krauklis waves. Krauklis waves are a type of guided wave that travel along the face of fluid-filled fractures. Krauklis waves can be excited by a number of sources including tube waves that are incident on the mouth of hydraulically connected fracture. Figure 9 shows a model of the Krauklis wave initiation from incident tube waves and subsequent propagation along the fracture face. Counter-propagating Krauklis waves in a fracture form standing waves that have resonant frequencies and decay rates dependent upon the fracture geometry (Liang et al., 2017). Therefore, if the resonate frequencies and decay rate can be measured using DAS for each perf cluster, these values could be used to help constrain the fracture geometries.

We believe that these Krauklis waves are in fact being excited by the tube waves following the perf shot and are observable on the DAS data. In Figure 10a we observe signals at each of the perf cluster locations in stage 26 resonating for hundreds of ms after the initial tube wave arrival. In Figure 9b, which shows the windowed section transformed from the space-time (t-x) domain to the space-frequency (f-x) domain, we see these resonate waves occur at specific frequencies at each perf cluster. Conversely, in stage 32, we do not see the same resonate signals in either the t-x or f-x domains along clusters 2-6, which, as discussed earlier, were not stimulated effectively. However, we do observe resonant signals at cluster 1 in stage 32, which did appear effectively stimulated. In the case of both cluster 1 from stage 32 and clusters 1-3 in stage 26, the resonant frequencies appear to be up to several thousand Hz and, according to the model presented in Liang

DOI:10.1190/geo2021-0276.1

et al. (2017), this indicates fracture lengths of up to only a few meters. Therefore, we are likely only observing the highly conductive area of the fracture in the near-wellbore region. Future work can build on these potential observations of Krauklis waves on DAS following the perf shot and use the resonate frequencies and decay rates to constrain fracture geometries.

Although the perf shot data can provide valuable insights, it is important to be aware of some potentially limiting factors of DAS that may affect the observations. First, although the DAS fiber cable is mounted to casing along the wellbore, there can be inconsistencies in the mechanical coupling among the DAS channels. This inconsistency may result in different channel responses and affect the reliability of the recorded amplitudes. The gauge length of the fiber can also be a limiting factor for DAS data. For waves propagating along the wellbore, if the wavelength is shorter than the gauge length, the recorded signal will be distorted (Bakulin et al., 2018). Since the tube waves in our dataset have a velocity of ~1500 m/s and the gauge length is estimated to be 1 m, the highest frequency that can be recorded accurately is 1500 Hz. Therefore, the high frequencies in our tube wave dataset are likely higher in amplitude than they appear. The last issue we will discuss is due to the dynamic range of the DAS measurements and the large amplitudes of tube waves near the perf gun. DAS records strain rate through the optical phase shift of the backscattered light from $-\pi$ to π between two sample intervals. When the strain rate exceeds this range, the recorded data will experience cycle skipping and the amplitudes will be recorded incorrectly. Figure 11 displays two traces from adjacent DAS channels following the stage 27 perf shot that we believe are affected by this dynamic range problem. In lower amplitude sections of these traces (before 10 ms and after 20 ms), the signals recorded on each channel are fairly coherent. However, in the higher amplitude portion of the traces (between 10-20 s) where the strain

DOI:10.1190/geo2021-0276.1

rate is higher, the signals are quite incoherent. We believe that this incoherency is a result of cycle skipping caused by the high strain rates within this window of time. However, in our data this phenomenon primarily affects the tube waves near the perf gun where the amplitudes are the largest and we do not believe it has a significant effect on the majority of the traces within the prior stage where the tube wave decay is measured. Although these limitations of DAS impact at the traces to various extents, we do not see evidence that the impact is great enough to significantly change the recorded trend of tube wave decay within a stage and we assert the calculated decay rates to be minimally affected.

From our analysis of the DAS data following the perf shot in this work, we identified several key items that we recommend further examining in future work. First, additional uses of DAS data recorded during the perf shot should be considered. Examples of these include the use of tube waves for plug failure identification, the use of Krauklis waves to constrain the highly conductive length of the fractures, and the incorporation of reflected tube waves for further assessment the near-wellbore connectivity. Second, we also recommend further researching both the limitations of the data and processing/acquisition strategies to improve data quality and enable a more quantitative analysis of tube wave decay in the future. Some examples of future research topics include studying the effects of gauge length on tube waves with different wave lengths, correcting for mechanical coupling differences along the fiber, and correcting/mitigating the dynamic range problem described previously. By addressing these limitations, the reliability and resolution of the data can be increased along with the insights provided.

CONCLUSION

DOI:10.1190/geo2021-0276.1

In this work, we introduced a number of previously unpublished observations from DAS recorded during the perf shot and demonstrated the potential value of the tube waves in this data for evaluating the hydraulic connectivity of induced fractures near the wellbore for each stage. The near-wellbore fracture connectivity is highly related to the production in unconventional wells, as it controls the flow of hydrocarbons from the far-field into the wellbore, but there are currently no established methods to evaluate it at the stage level. However, we illustrated how the decay rate of tube waves excited by the perf shot and recorded on DAS can be related to the fracture connectivity for each stage and correlated with the effectiveness of the treatment. Although many applications of DAS have been developed for evaluating induced fractures in the far-field, this method is one few that exist for evaluating the near-wellbore region. Since the perf shot is typically recorded on DAS for depth calibration purposes, this method also presents a cost-effective way to repurpose this data and provide an additional fracture diagnostic measurement. There may even be further applications for the DAS perf shot data which we discussed such as plug failure evaluation and constraining the highly conductive length of the fracture using Krauklis waves. In this way, this work shows how the perf shot data on DAS presents a unique opportunity to obtain new insights from a dataset that is commonly obtained yet highly underutilized.

ACKNOWLEDGMENTS

We would like to thank Civitas Resources (merged with HighPoint Resources) for providing data as well as mentorship for this project. We also thank the sponsors of Reservoir Characterization Project (RCP) at Colorado School of Mines for enabling this research to be conducted. Lastly, we thank the RCP faculty, staff, and students for their continuing support.

REFERENCES

Bakku, S. M. Fehler, and D. Burns, 2013, Fracture compliance estimation using borehole tube waves: Geophysics, 78, no. 4, doi: https://doi.org/10.1190/geo2012-0521.1

Bakulin, A., I. Silvestrov, and R. Pevzner, 2018, Surface seismic with DAS: looking deep and shallow at the same time: 88th Annual International Meeting, SEG, Expanded Abstracts, 16-20, doi: https://doi.org/10.1190/segam2018-2995870.1

Bergery, G., Z. Zhang, J. Du, D. Diller, T. Shuck, and B. Fish, 2017, The plug drum effect, or why your microseismic events may not be where you think they are: Unconventional Resources Technology Conference (URTeC), doi: https://doi.org/10.15530/urtec-2017-2691531

Binder, G., and D. Chakraborty, 2019, Detecting microseismic events in downhole distributed acoustic sensing data using convolutional neural networks: 89th Annual International Meeting, SEG, Expanded Abstracts, 4864-4868, doi: https://doi.org/10.1190/segam2019-3214863.1

Binder, G., A. Titov, D. Tamayo, J. Simmons, A. Tura, G. Byerley, and D. Monk, 2019, Time-lapse seismic monitoring of individual hydraulic frac stages using a downhole distributed acoustic sensing array: Unconventional Resources Technology Conference (URTeC), doi: https://doi.org/10.15530/urtec-2019-409

Dunham, E., J. Zhang, Y. Quan, J. Harris, and K. Mace, 2017, Hydraulic fracture conductivity inferred from tube wave reflections: 87th Annual International Meeting, SEG, Expanded Abstracts, 947-952, doi: https://doi.org/10.1190/segam2017-17664595.1

Hartog, A. H., 2017, An introduction to distributed optical fibre sensors: CRC Press.

Holley, E., V. Martysevich, K. Cook, and S. Gale, 2020, Using automation while pumping to improve stimulation uniformity and consistency: a series of case studies: SPE Hydraulic Fracturing Technology Conference and Exhibition, doi: https://doi.org/10.2118/199742-MS

Holzhausen, G., and R. Gooch, 1985, Impedance of hydraulic fractures: its measurement and use for estimating fracture closure pressure and dimensions: SPE/DOE Low Permeability Gas Reservoirs Symposium, doi: https://doi.org/10.2118/13892-MS

Hunziker, J., A. Greenwood, S. Minato, N. D. Barbosa, E. Caspari, and K. Holliger, 2019, Bayesian full-waveform inversion of tube waves to estimate fracture aperture and compliance: 81st EAGE Conference and Exhibition, doi: https://doi.org/10.5194/se-2019-183

Jin, G., and B. Roy, 2017, Hydraulic-fracture geometry characterization using low-frequency DAS signal: The Leading Edge, 36, no. 12, 975–980, doi: https://doi.org/10.1190/tle36120975.1.

Li, Y., H. Wang, M. Fehler, and Y. Fu, 2017, Wavefield characterization of perforation shot signals in a shale gas reservoir: Physics of the Earth and Planetary Interiors, 267, 31-40, doi: https://doi.org/10.1016/j.pepi.2017.04.003.

Liang, C., O. O'Reilly, E. M. Dunham, and D. Moos, 2017, Hydraulic fracture diagnostics from Krauklis wave resonance and tube wave reflections: Geophysics, 82, no. 3, doi: https://doi.org/10.1190/geo2016-0480.1.

Sookprasong, P. A., R. S. Hurt, C. C. Gill, and R. F. LaFollette, 2014, Fiber optic DAS and DTS in multicluster, multistage horizontal well fracturing: interpreting hydraulic fracture initiation and propagation through diagnostics: SPE Annual Technical Conference and Exhibition, doi: https://doi.org/10.2118/170723-MS

Ugueto, G., P. Huckabee, M. Wojtaszek, T. Daredia, and A. Reynolds, 2019, New near-wellbore insights from fiber optics and downhole pressure gauge data: SPE Hydraulic Fracturing Technology Conference and Exhibition, doi: https://doi.org/10.2118/194371-MS

Zhang, S., A. Titov, V. Jayaram, H. Bello, R. Hurt, and G. Jin, 2021, DAS recorded body and tube wave generated by perforation shots: analysis and numerical modeling for completion monitoring and reservoir characterization: Unconventional Resources Technology Conference (URTeC), doi: https://doi.org/10.15530/urtec-2021-5140

DOI:10.1190/geo2021-0276.1

Zlatev, P., E. Poeter, and J. Higgins, 1988, Physical modeling of the full acoustic waveform in a fractured, fluid-filled borehole: Geophysics, 53, no. 9, doi: https://doi.org/10.1190/1.1442562

FIGURES CAPTIONS

Figure 1. Simplified model of tube wave decay following the perf shot due to the hydraulic impedance contrast of induced fractures along the perf clusters in the prior stage.

Figure 2. Example of a typical wavefield and RMS amplitude profile observed on DAS following the perf shot. The amplitudes are shown using a color scale from yellow (positive) to purple (negative). The left panel shows an expanded view of dashed box on the right panel with the P-wave and tube wave first arrivals labeled as well as the locations of the plug seat of the current stage (orange) and plug of the prior stage (red) overlain.

Figure 3. Diagram of the steps (performed in order from left to right) in the workflow used to quantify the tube wave decay rate for each stage. (a) Linear moveout (LMO) applied in both directions from the perf gun at the tube wave velocity (1494 m/s). (b) 100 ms time window used after LMO to isolate the tube wave energy from the body wave energy. (c) Log of the average amplitude calculated within the time window for each channel as well as the line fit between the plug of the current stage and the plug of the previous stage.

Figure 4. Example of two stages with very different tube wave decay rates. (a) Wavefield (after LMO) in stage 22 following a perf shot from stage 23. (b) Log of the average amplitudes

DOI:10.1190/geo2021-0276.1

recorded in stage 22 within the 100 ms window shown in panel a. (c) Wavefield (after LMO) in stage 32 following a perf shot from stage 33. (d) Log of the average amplitudes recorded in stage 32 within the 100 ms window shown in panel c.

Figure 5. Calculated uniformity index for stage 22 and 32 and percent of total injected fluid allocated to each cluster as estimated from high frequency DAS during completion.

Figure 6. The temperature profile from DTS during the treatments for stages 30-32. The treatment fluid, which has a much lower temperature than the reservoir, appears as a low temperature anomaly in the stage during the treatment and then gradually warms back to the reservoir temperature overtime.

Figure 7. Phase power of the high-frequency (500-5000Hz) DAS during the completion of stage 32. The color scale shows the phase power from high (red) to low (blue) and the perf cluster locations for stages 32 and 31 and shown by the horizontal dashed lines.

Figure 8. Identification of plug leakage using tube waves. (a) Wavefield in stages 31 and 30 following a perf shot from stage 32. (b) Log of the average amplitudes recorded in stages 31 and 30 within the 100 ms window shown in (a). (c) Wavefield in stage 32 following a perf shot from stage 33. (d) Log of the average amplitudes recorded in stage 32 within the 100 ms window shown in (c).

DOI:10.1190/geo2021-0276.1

Figure 9. Illustration of Krauklis waves (initiated by the incident tube waves) traveling up and down the conductive length of the induced fracture at a frequency and decay rate dependent on the geometry of the fracture.

Figure 10. Example of suspected Krauklis waves following the perf shot and recorded on DAS. (a) Wavefield in stage 26 following a perf shot from stage 27. (b) Transformation of the windowed section in (a) from the time-space domain to the frequency space domain. (c) Wavefield in stage 32 following a perf shot from stage 33. (d) Transformation of the windowed section in (c) from the time-space domain to the frequency space domain.

Figure 11. Traces from two adjacent DAS channels following the perf shot from stage 27 (wavefield shown in Figure 9a).

DOI:10.1190/geo2021-0276.1

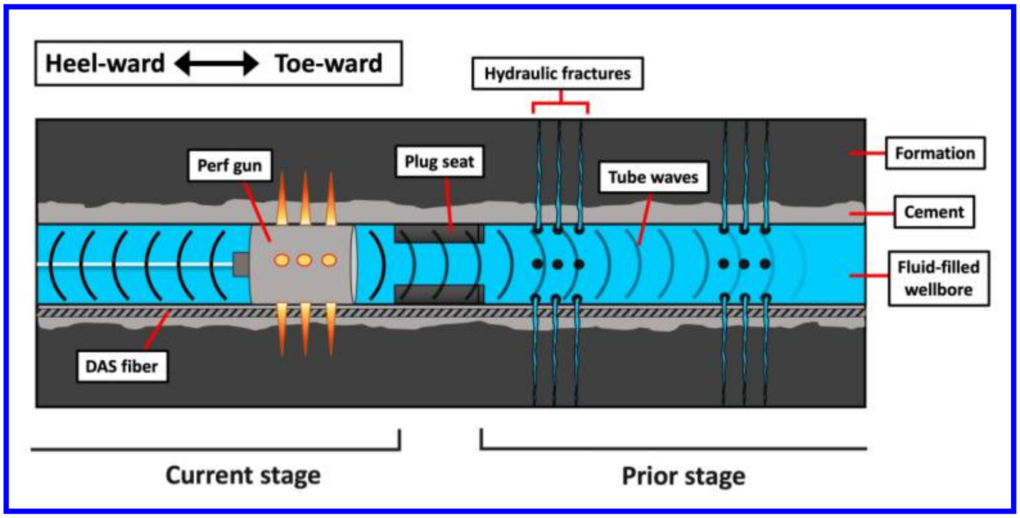

Figure 1. Simplified model of tube wave decay following the perf shot due to the hydraulic impedance contrast of induced fractures along the perf clusters in the prior stage.

301x149mm (300 x 300 DPI)

DOI:10.1190/geo2021-0276.1

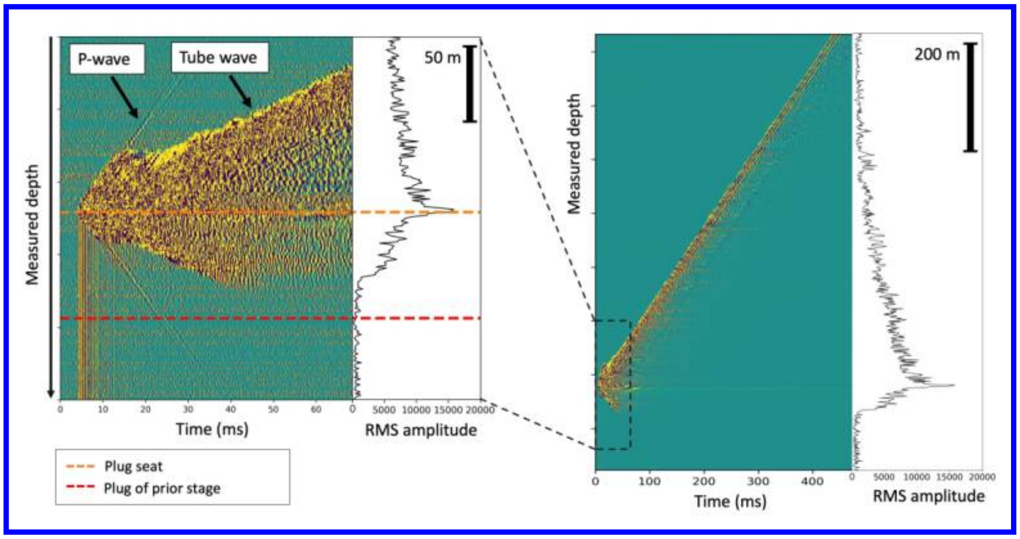

Figure 2. Example of a typical wavefield and RMS amplitude profile observed on DAS following the perf shot. The amplitudes are shown using a color scale from yellow (positive) to purple (negative). The left panel shows an expanded view of dashed box on the right panel with the P-wave and tube wave first arrivals labeled as well as the locations of the plug seat of the current stage (orange) and plug of the prior stage (red) overlain.

311x160mm (300 x 300 DPI)

DOI:10.1190/geo2021-0276.1

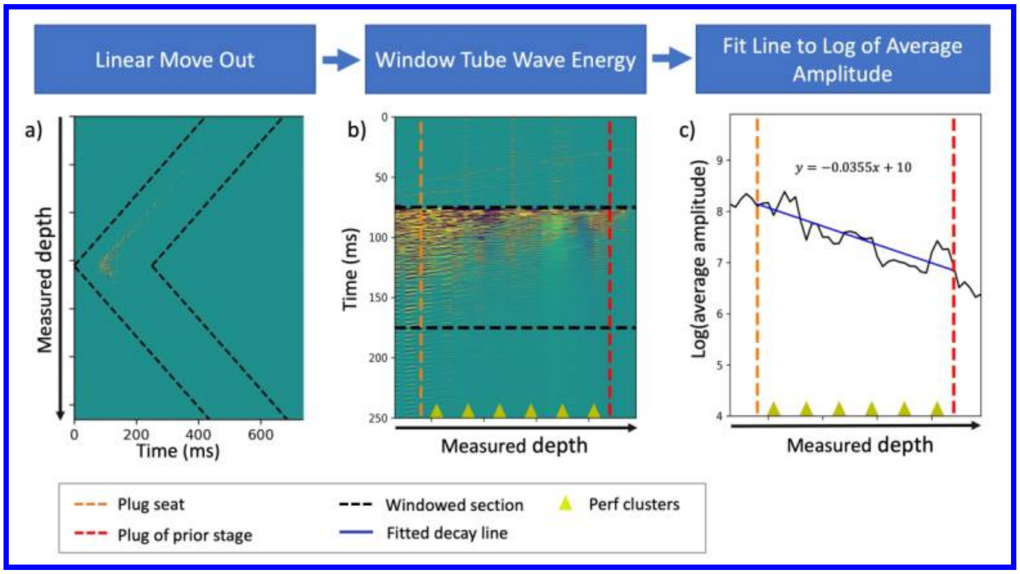

Figure 3. Diagram of the steps (performed in order from left to right) in the workflow used to quantify the tube wave decay rate for each stage. (a) Linear moveout (LMO) applied in both directions from the perf gun at the tube wave velocity (1494 m/s). (b) 100 ms time window used after LMO to isolate the tube wave energy from the body wave energy. (c) Log of the average amplitude calculated within the time window for each channel as well as the line fit between the plug of the current stage and the plug of the previous stage.

270x149mm (300 x 300 DPI)

DOI:10.1190/geo2021-0276.1

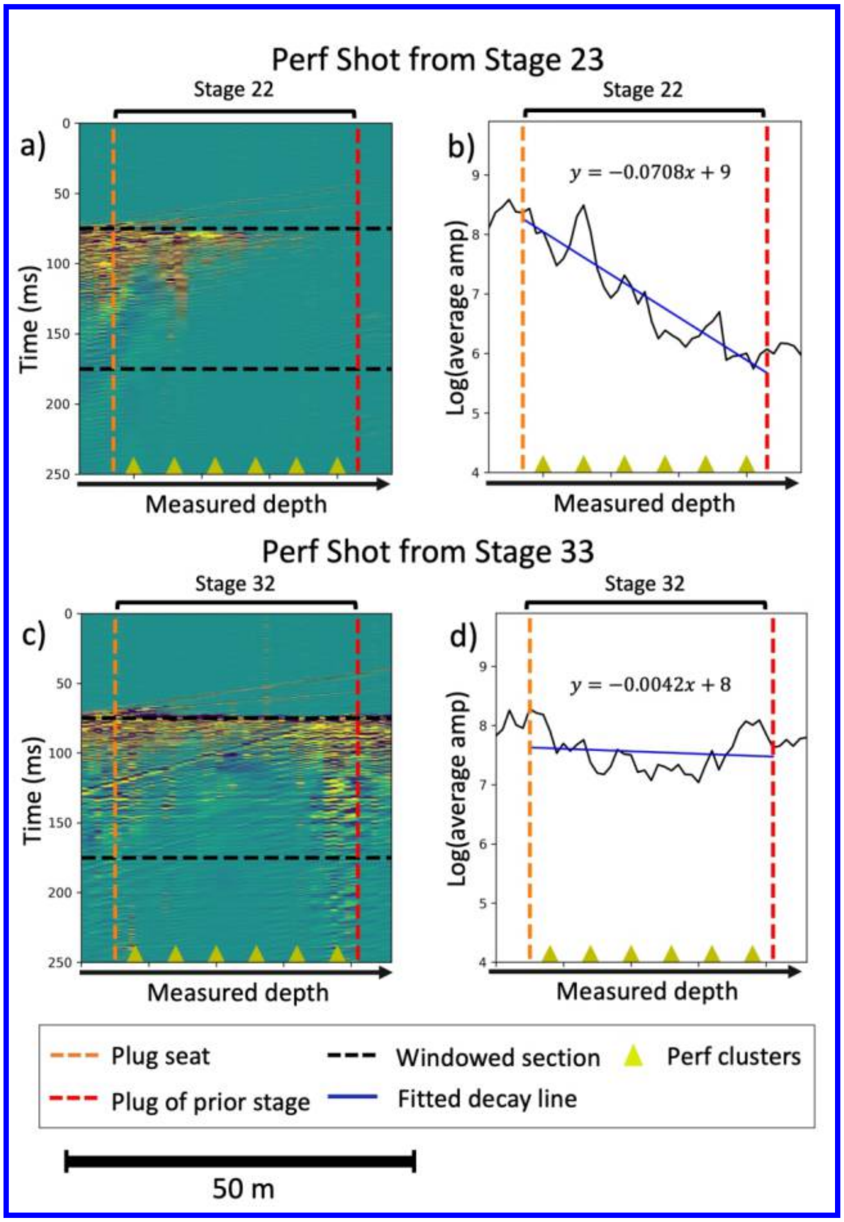

Figure 4. Example of two stages with very different tube wave decay rates. (a) Wavefield (after LMO) in stage 22 following a perf shot from stage 23. (b) Log of the average amplitudes recorded in stage 22 within the 100 ms window shown in panel a. (c) Wavefield (after LMO) in stage 32 following a perf shot from stage 33. (d) Log of the average amplitudes recorded in stage 32 within the 100 ms window shown in panel c.

150x218mm (300 x 300 DPI)

DOI:10.1190/geo2021-0276.1

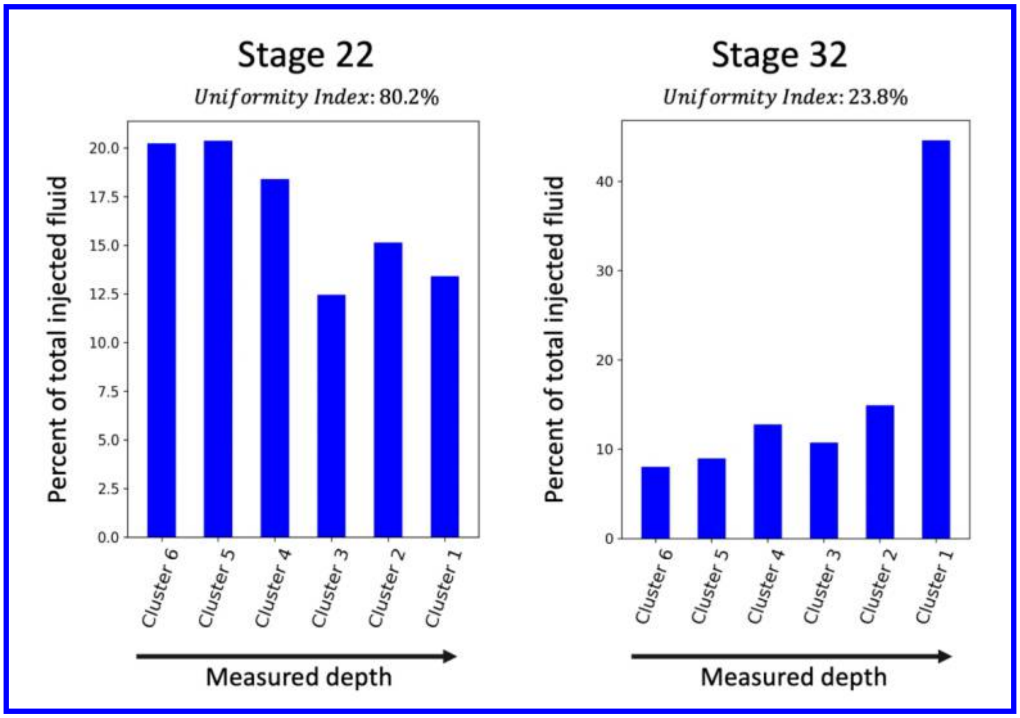

Figure 5. Calculated uniformity index for stage 22 and 32 and percent of total injected fluid allocated to each cluster as estimated from high frequency DAS during completion.

177x123mm (300 x 300 DPI)

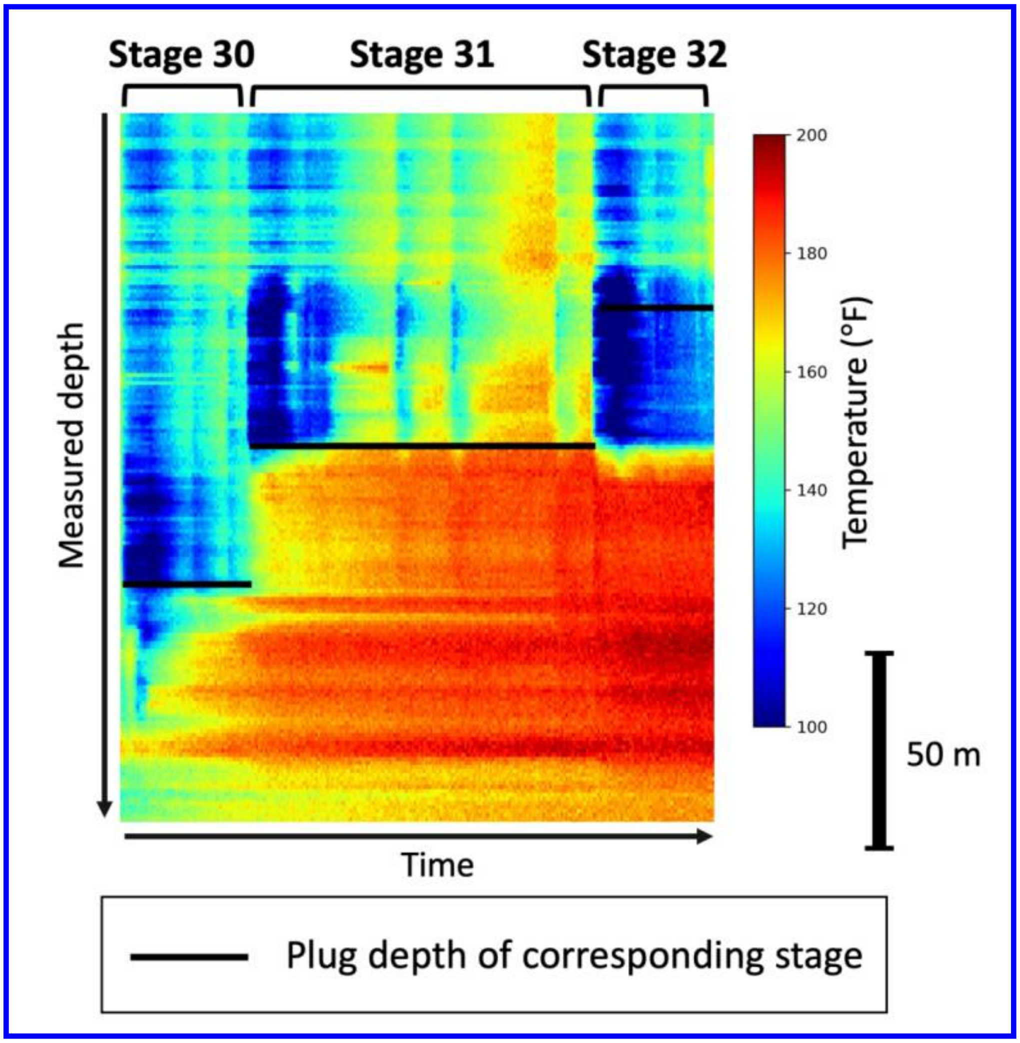

Figure 6. The temperature profile from DTS during the treatments for stages 30-32. The treatment fluid, which has a much lower temperature than the reservoir, appears as a low temperature anomaly in the stage during the treatment and then gradually warms back to the reservoir temperature overtime.

152x155mm (300 x 300 DPI)

DOI:10.1190/geo2021-0276.1

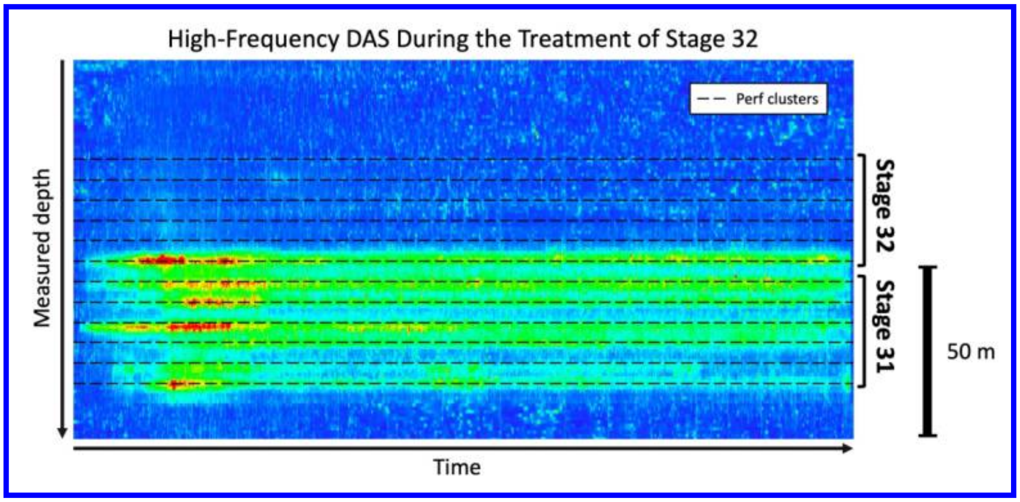

Figure 7. Phase power of the high-frequency (500-5000Hz) DAS during the completion of stage 32. The color scale shows the phase power from high (red) to low (blue) and the perf cluster locations for stages 32 and 31 and shown by the horizontal dashed lines.

236x113mm (300 x 300 DPI)

DOI:10.1190/geo2021-0276.1

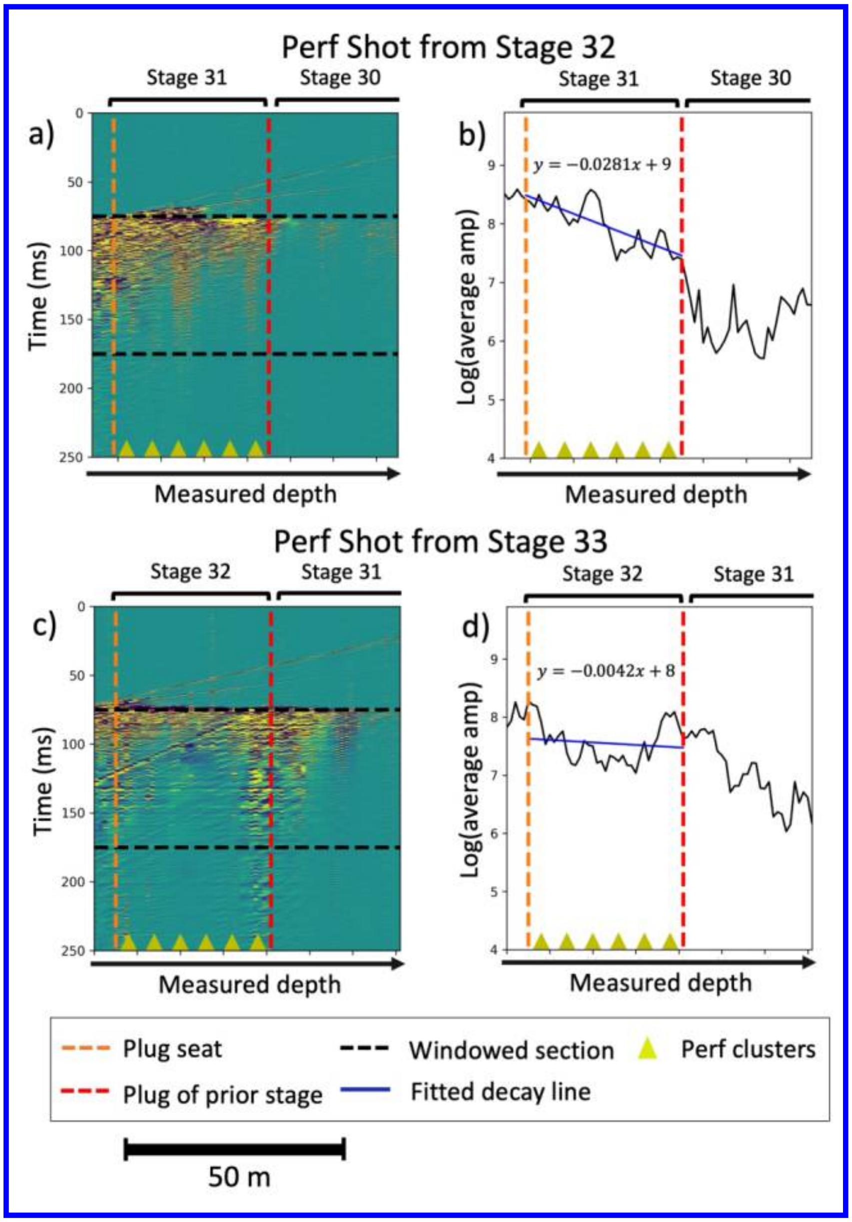

Figure 8. Identification of plug leakage using tube waves. (a) Wavefield in stages 31 and 30 following a perf shot from stage 32. (b) Log of the average amplitudes recorded in stages 31 and 30 within the 100 ms window shown in (a). (c) Wavefield in stage 32 following a perf shot from stage 33. (d) Log of the average amplitudes recorded in stage 32 within the 100 ms window shown in (c).

151x217mm (300 x 300 DPI)

DOI:10.1190/geo2021-0276.1

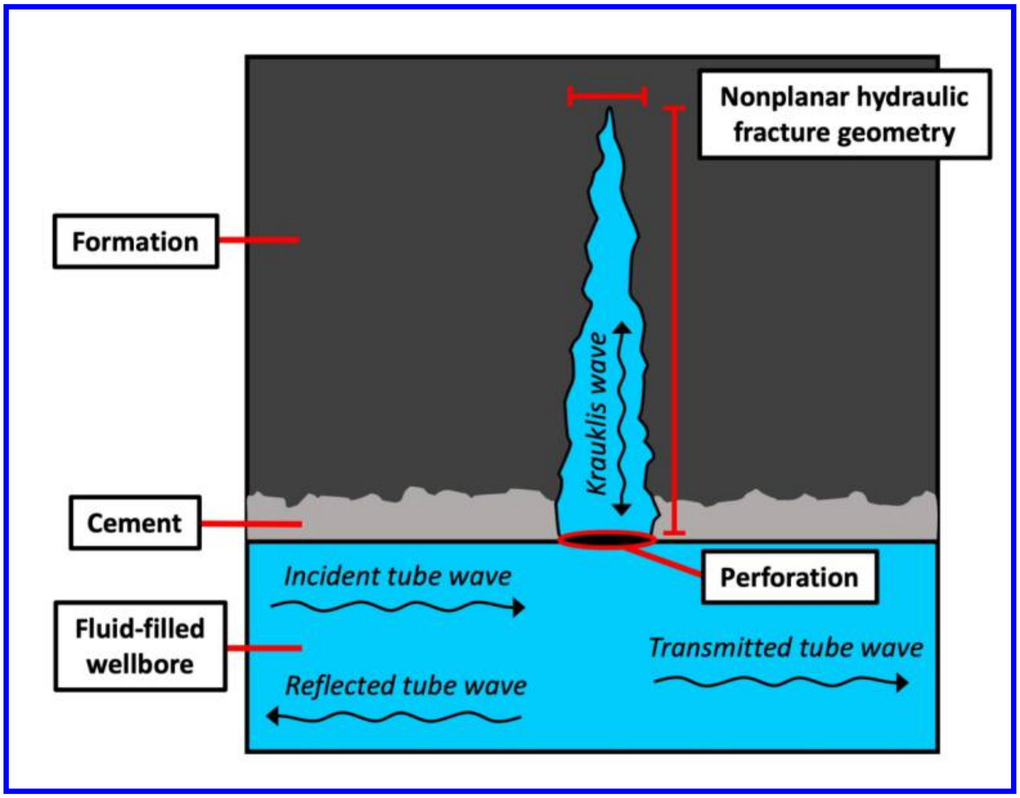

Figure 9. Illustration of Krauklis waves (initiated by the incident tube waves) traveling up and down the conductive length of the induced fracture at a frequency and decay rate dependent on the geometry of the fracture.

166x129mm (300 x 300 DPI)

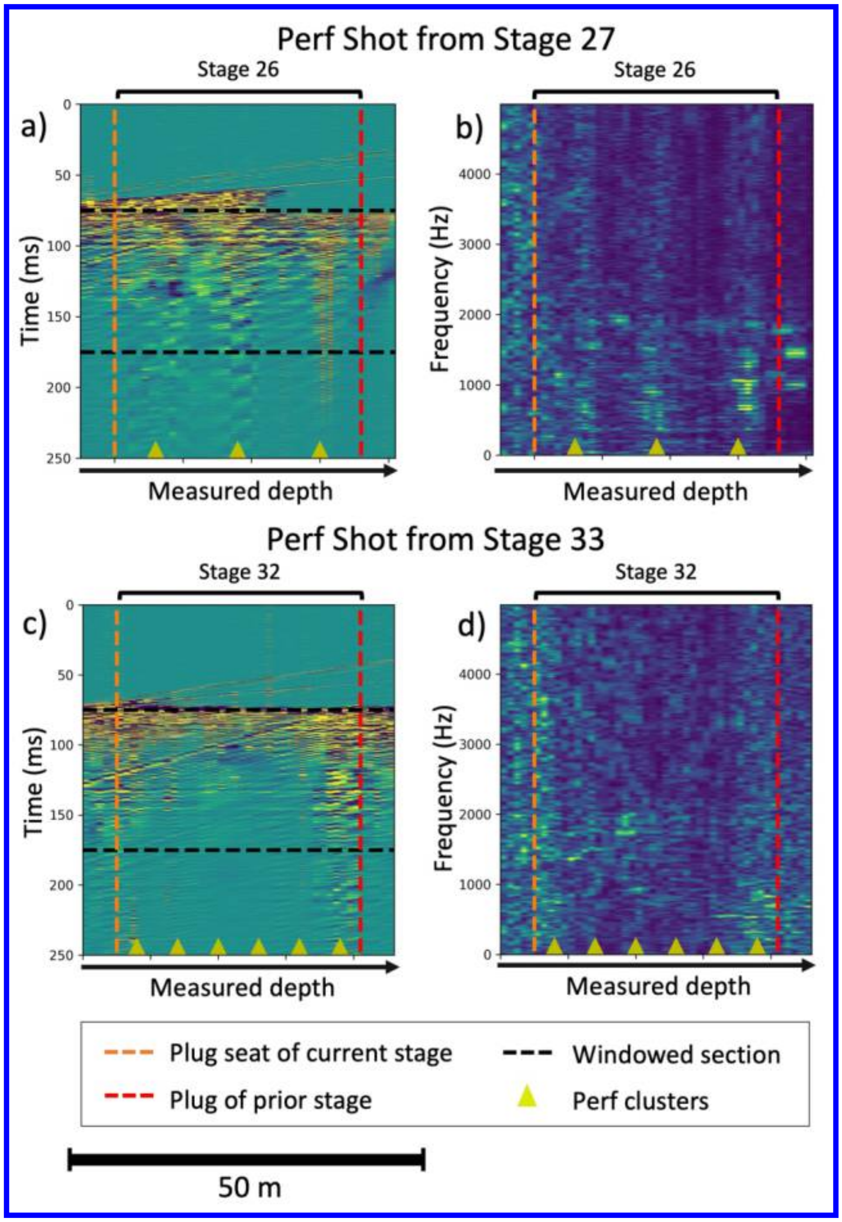

Figure 10. Example of suspected Krauklis waves following the perf shot and recorded on DAS. (a) Wavefield in stage 26 following a perf shot from stage 27. (b) Transformation of the windowed section in (a) from the time-space domain to the frequency space domain. (c) Wavefield in stage 32 following a perf shot from stage 33. (d) Transformation of the windowed section in (c) from the time-space domain to the frequency space domain.

147x214mm (300 x 300 DPI)

DOI:10.1190/geo2021-0276.1

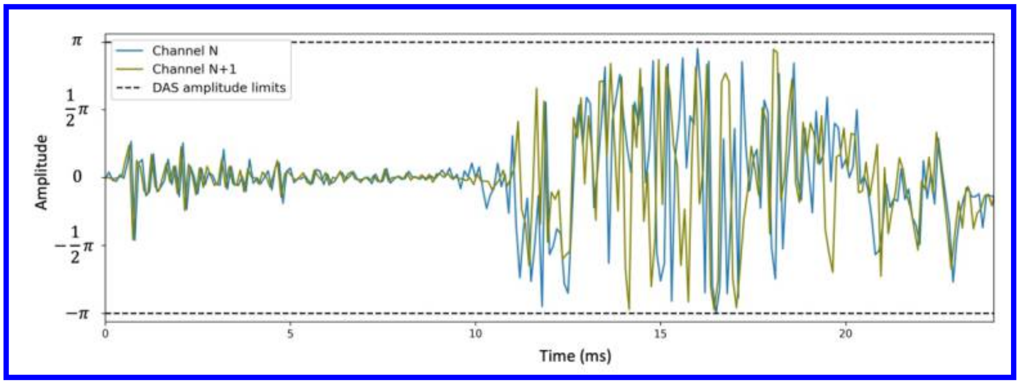

Figure 11. Traces from two adjacent DAS channels following the perf shot from stage 27 (wavefield shown in Figure 9a).

276x100mm (300 x 300 DPI)

DOI:10.1190/geo2021-0276.1

DATA AND MATERIALS AVAILABILITY

Data associated with this research are confidential and cannot be released.

DOI:10.1190/geo2021-0276.1